Mitigation of Striping Noise in ATMS Calibration Counts by Symmetric Filters

XIAOXU TIAN AND XIAOLEI ZOU

Earth System Science Interdisciplinary Center, University of Maryland, College Park, College Park, Maryland

(Manuscript received 30 October 2018, in final form 11 April 2019)

ABSTRACT

Global observations from the Advanced Technology Microwave Sounder (ATMS) onboard the *Suomi National Polar-Orbiting Partnership* satellite are affected by striping-patterned noise. An optimal symmetric filter method to mitigate the striping noise in warm counts, cold counts, warm load temperatures, and scene counts instead of antenna temperatures is developed and tested in this study. The optimal filters are developed based on the results free of striping noise obtained with a striping noise detecting method by combining the principal component analysis and the ensemble empirical mode decomposition. The two-point algorithm is then used to calculate antenna temperatures with warm counts, cold counts, warm load temperatures, and scene counts before and after applying the optimal filters. The necessity of applying the striping noise mitigation to the scene counts besides the calibration counts (warm and cold counts) is also shown. This explains why the traditional method to smooth only calibration counts has failed to remove the ATMS striping noise. The optimal filters proposed in this study, which remove the high-frequency striping noise without altering low-frequency weather signals, outperform the conventional boxcar filters adopted in the current operational ATMS calibration system.

1. Introduction

The *Suomi National Polar-Orbiting Partnership* (*SNPP*) satellite was successfully launched into a sun-synchronous polar orbit on 28 October 2011 with an equator crossing time of 1330 local time. The Advanced Technology Microwave Sounder (ATMS) on-board *SNPP* is a new cross-track and line-scanning microwave radiometer. The ATMS combines the functionalities of the previous Advanced Microwave Sounding Unit A (AMSU-A) and Microwave Humidity Sounder (MHS) into a single instrument. The ATMS is the most advanced and state-of-the-art satellite-based microwave instrument that simultaneously provides temperature- and humidity-sounding information at the same 96 field-of-view (FOV) Earth view locations. Compared with its predecessors AMSU-A and MHS, the ATMS has several improvements including a wider swath width, additional sounding channels, and smaller noise equivalent delta temperatures (Weng et al. 2013b). Kim et al. (2014) evaluated the on-orbit performance of the ATMS and showed that the radiometric sensitivity was well maintained and that the

radiometric accuracy met or even surpassed expectations. Many studies have focused on the calibration and validation of ATMS observations where radiances simulated by an atmospheric radiative transfer model with global numerical weather prediction (NWP) datasets (*B*) serve as references for observed radiances (*O*) (Weng et al. 2012, 2013b; Zou et al. 2014; Tian et al. 2018).

Bormann et al. (2013) discovered that striping-patterned noise was detectable in the differences between observations and simulations ($O - B$), suggesting a contamination of striping noise in ATMS observations. The diagnosis and mitigation of high-frequency striping noise are challenging tasks that must be undertaken to fully explore the potential of the ATMS to NWP and climate studies (Zou et al. 2013; Tian and Zou 2016, 2018; Zou and Tian 2018). Wu and Huang (2009) and Wu et al. (2009) proposed an ensemble empirical mode decomposition (EEMD) method for extracting from raw data different frequency components. For a given time series, the EEMD method uses information about the minima and maxima of the riding waves in the set of noise-added ensemble data time series itself and successively extracts the oscillatory components called intrinsic mode functions (IMFs) from the highest to the lowest frequencies. Unlike the
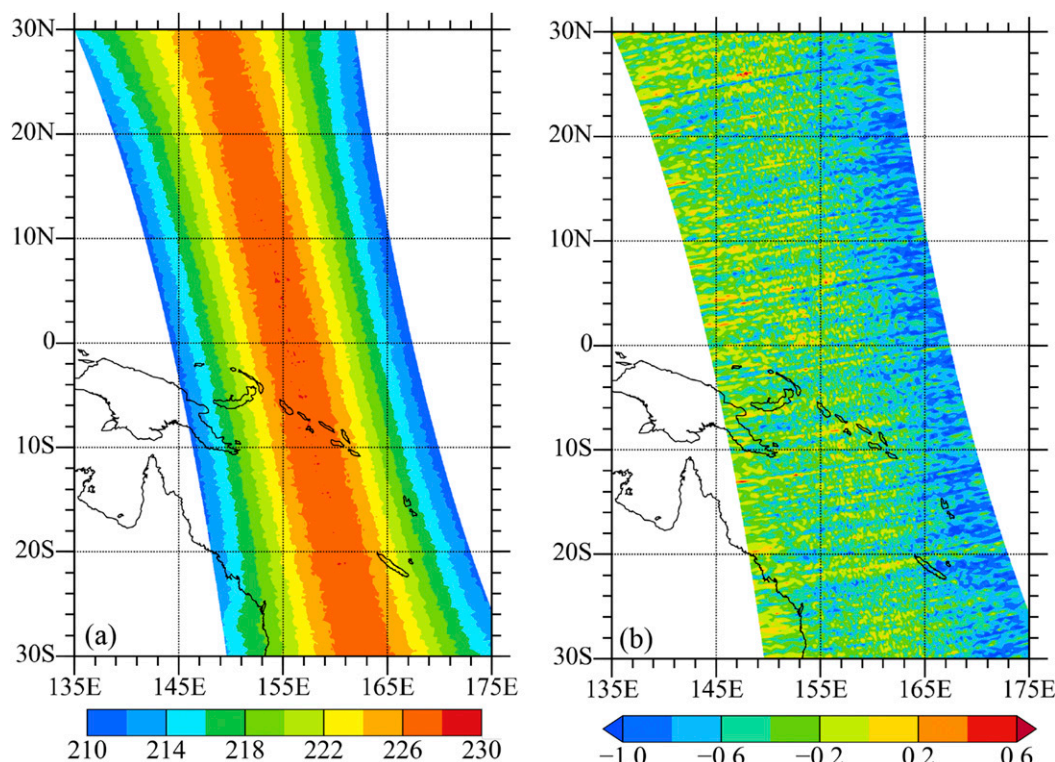
FIG. 1. (a) Brightness temperatures at channel 8 in the ascending node on 24 Feb 2012. (b) The differences of brightness temperatures at channel 8 between the observed and those simulated by the Community Radiative Transfer Model on 24 Feb 2012.

preexisting harmonic base functions of the Fourier frequency transform, the IMFs of the EEMD method are locally adaptive basis functions extracted directly from the data, making them more physically representative. The EEMD method also works for data series representing nonlinear processes. Qin et al. (2013) pointed out that striping noise is contained in the first principle component (PC) generated from the principal component analysis (PCA) of ATMS observations and applied the EEMD method to extract the ATMS striping noise. This method cannot only remove the striping noise in temperature-sounding channels, but also humidity channels for which the striping phenomenon is not visible in $O - B$ distributions. Specifically, the first three high-frequency IMFs are extracted from the first PC coefficient of antenna temperatures. The removed striping noise has a frequency range centered at $\sim 10^{-2}\,\mathrm{s}^{-1}$ and magnitudes of $\sim 0.3\,\mathrm{K}$ for ATMS temperature channels and 1 K for ATMS humidity channels. Zou et al. (2017) and Zou and Tian (2019) further refined the PCA/EEMD method proposed by Qin et al. (2013) to make it also applicable to the window channels of the ATMS onboard both the *SNPP* satellite and the *National*

Oceanic and Atmospheric Administration (*NOAA*)-20 satellite launched in 2017.

A detailed description of converting raw data counts to antenna temperatures through the ATMS calibration process is given in Weng et al. (2013b) and in the ATMS advanced technical baseline documentation (GSFC 2011). The two-point calibration involves converting Earth scene counts into antenna temperatures through a linear relationship defined by warm counts, cold counts, warm load temperature, and cold space temperatures. A quadratic term accounting for the nonlinear relationship between antenna temperatures and counts is also added. Conventionally, radiometric calibration error sources include target emissivity, measurement uncertainty, the Rayleigh approximation, and antenna sidelobe interception (Weng et al. 2013a). Figure 1 shows antenna temperature observations (Fig. 1a) and differences of antenna temperatures between observations O and model simulations B (Fig. 1b) for ATMS channel 8 over a swath at the ascending node of *SNPP* on 24 February 2012. An along-track striping noise feature, with its magnitude varying randomly in the along-track direction, can be seen in both the observations
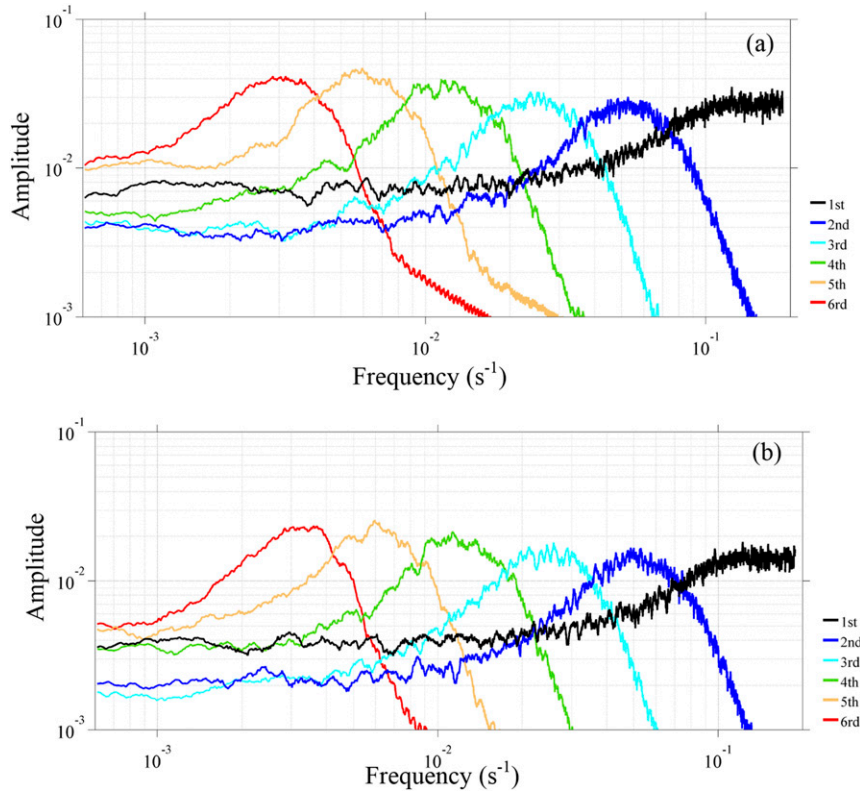
FIG. 2. Fourier spectra with 81-point running means for the first six IMFs of (a) warm counts and (b) cold counts at channel 8 on 24 Feb 2012.

(Fig. 1a) and the $O - B$ difference (Fig. 1b) fields. Warm counts, cold counts, and warm load temperatures are traditionally smoothed in an operational system using either a triangular or a boxcar filter to reduce the effect of radiometric instrument errors on antenna temperatures, while the scene counts are not smoothed. To more effectively suppress the instrument error due to noise, in this study, a new set of optimal filters for ATMS warm
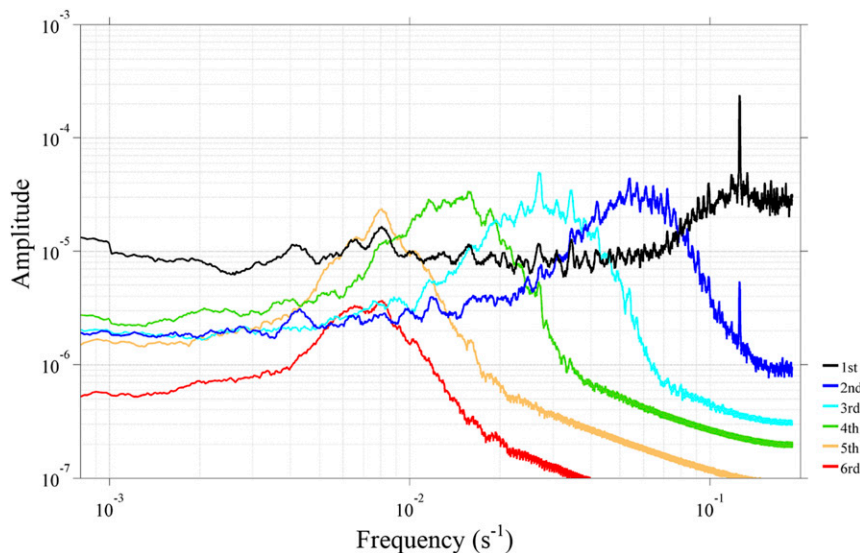

FIG. 3. As in Fig. 2, but for warm load temperatures. Five IMFs are removed.
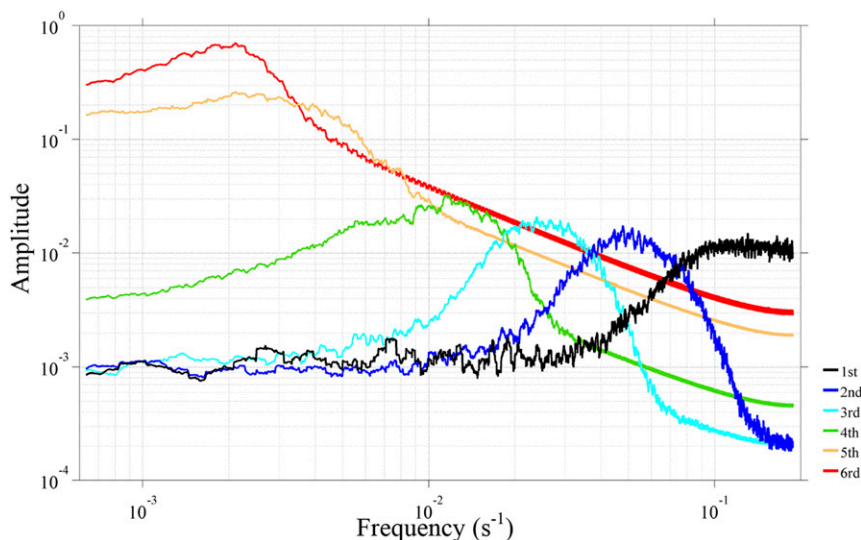
FIG. 4. As in Fig. 2, but for the first PC coefficient of scene counts at channel 8. Three IMFs are removed.

counts, cold counts, warm load temperature, and scene counts is thus proposed. Section 2 briefly describes ATMS instrument characteristics and the two-point calibration. Theoretical derivations of the weighting coefficients of the optimal filters are provided in section 3. Section 4 presents numerical results of the optimal filters and the characteristics of the striping noise removed by the optimal filters. A summary of this study is finally given in section 5.

2. ATMS instrument and observation features

a. ATMS channel characteristics

The ATMS is a cross-track, line-scanning sensor. It takes 2.67 s to complete one scan cycle, which contains 96 FOVs for all 22 ATMS microwave temperature- and humidity-sounding channels. With a sampling interval of 1.11°, the scan angle of the outmost FOV is 52.7°. ATMS channels 1–3 and 5–16 have similar central frequencies as

TABLE 1. Channel frequencies, peak weighting functions (WFs), filter spans (FSs) of optimal striping filters for ATMS warm counts and cold counts, and scene counts.

| Channel No.	Central frequency (GHz)	Peak WF (hPa)	Warm count FS (N)	Cold count FS (N)	No. of IMFs removed	FS (N)
1	23.8	Surface	8	8	2	14
2	31.4	Surface	8	8	2	14
3	50.3	Surface	10	10	3	23
4	51.76	950	10	10	3	23
5	52.8	850	8	10	3	18
6	53.596 ± 0.115	700	8	10	3	17
7	54.4	400	8	10	3	19
8	54.94	250	8	10	3	17
9	55.5	200	10	10	3	17
10	57.2903	100	8	10	3	16
11	57.2903 ± 0.115	50	10	10	3	18
12	57.2903	25	10	10	3	18
13	57.2903 ± 0.322	10	10	10	3	18
14	57.2903 ± 0.322 ± 0.010	5	10	10	3	20
15	57.2903 ± 0.322 ± 0.004	2	10	10	3	17
16	88.2	Surface	8	8	2	16
17	165.5	Surface	8	8	3	23
18	183.31 ± 7	800	8	8	3	22
19	183.31 ± 4.5	700	8	8	3	22
20	183.31 ± 3	500	8	8	3	22
21	183.31 ± 1.8	400	8	8	3	22
22	183.31 ± 1.0	300	8	8	3	23
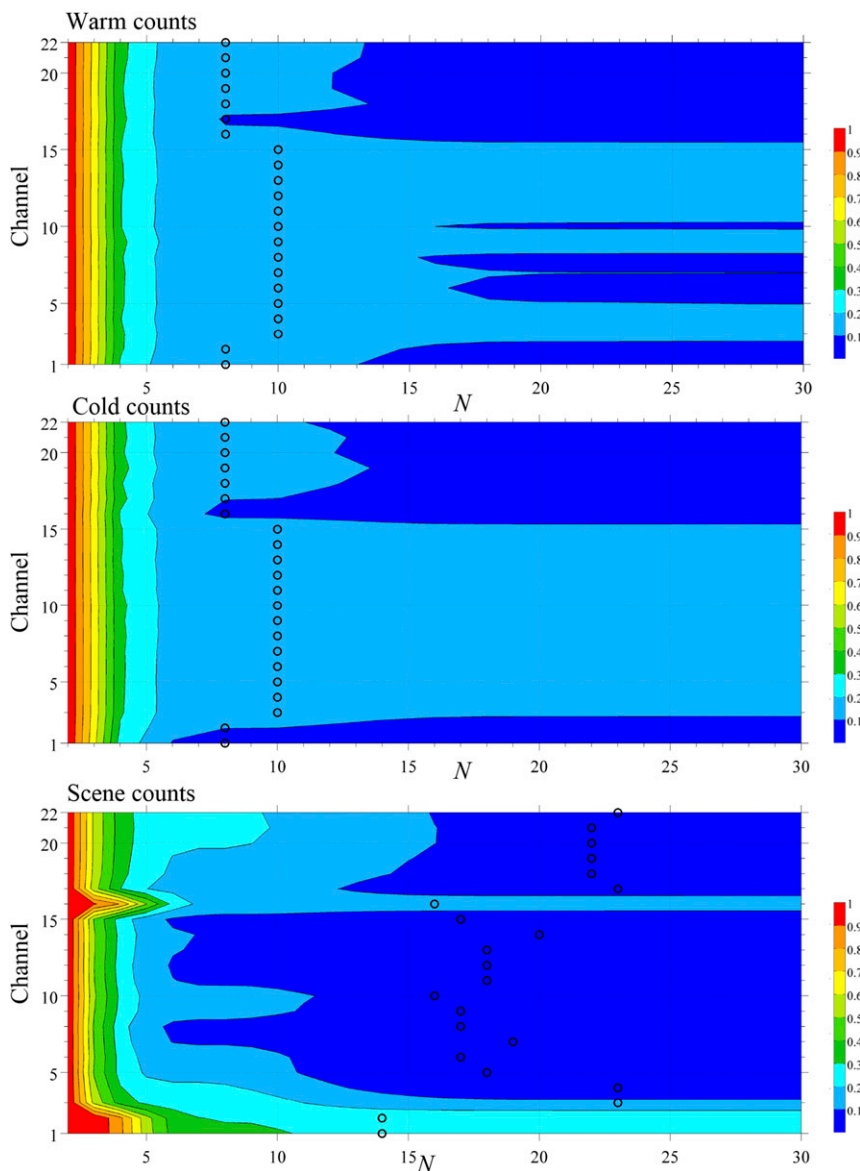
FIG. 5. Normalized cost function as a function of filter span N for (top) warm counts, (middle) cold counts, and (bottom) scene counts. The number of scanlines involved in the optimal filter is indicated by circles.

channels 1–15 of the traditional microwave temperature-sounding instrument AMSU-A. ATMS channels 17–22 contain channels with similar central frequencies as the five channels from the traditional humidity-sounding instrument MHS. Compared with its predecessors AMSU-A and MHS, the ATMS has an extra temperature channel 4 with its weighting function located in the lower troposphere and two new humidity channels 19 and 21. The swath width of the ATMS is 2500 km, which is wider than both AMSU-A and MHS swath widths, leaving almost no data gaps between two neighboring swaths over the entire globe.

The beam widths of channels 1–2, 3–16, and 17–22 are 5.2°, 2.2°, and 1.1°, respectively.

b. Derivation of antenna temperatures from raw counts

During each ATMS scanning cycle, the antenna first scans the Earth scene, then cold space, and finally the blackbody warm target (Weng et al. 2013b) to record the measured scene counts, warm counts, and cold counts when these three segments are completed. The antenna temperatures can be derived from the measured raw counts based on the following two-point calibration equations:
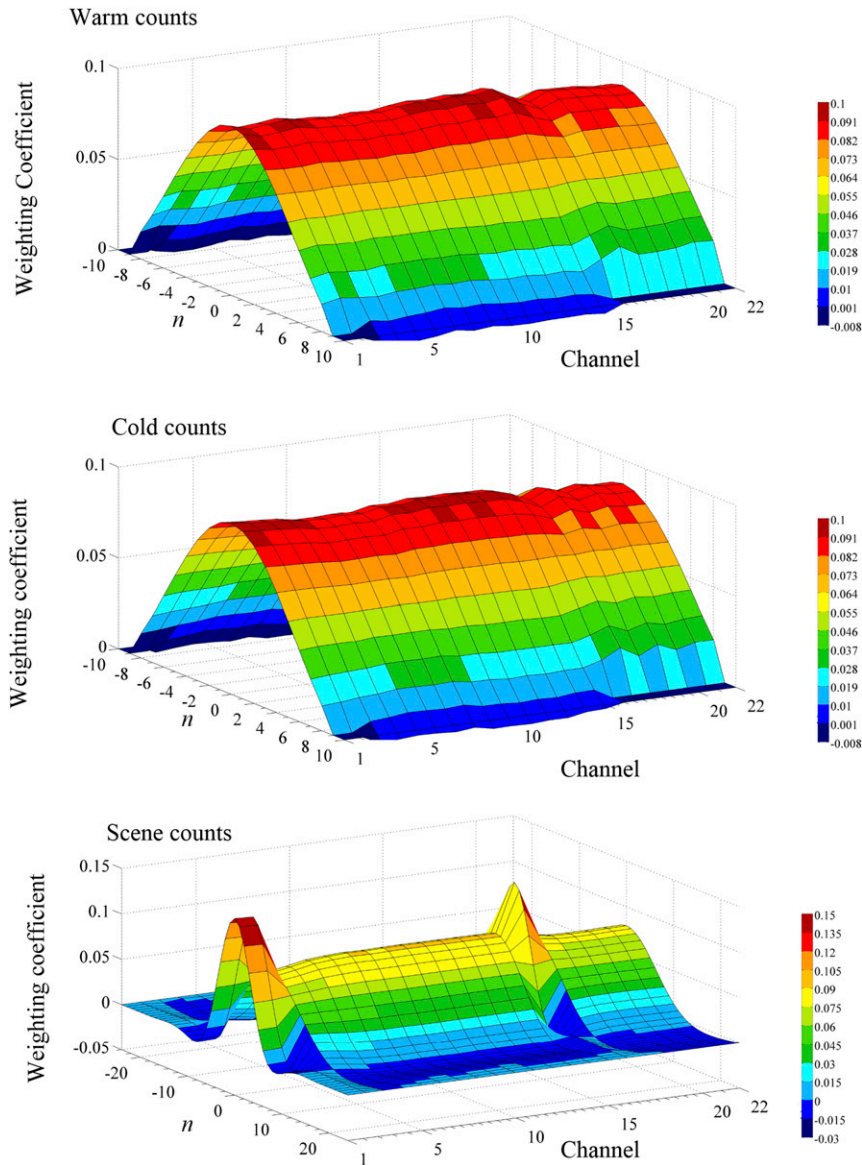
FIG. 6. Weighting coefficients of optimal filters for (top) warm counts, (middle) cold counts, and (bottom) scene counts.

$$T_{b,\text{ch}}(k,i) \equiv T_{\text{ch}}^w(k) + [G_{\text{ch}}(k)]^{-1}[C_{\text{ch}}^s(k,i) - C_{\text{ch}}^w(k)]$$

$$+ Q_{\text{ch}}(k,i),$$

$$G_{\text{ch}}(k) = \frac{\overline{C}_{\text{ch}}^w(k) - \overline{C}_{\text{ch}}^c(k)}{\overline{T}_{\text{ch}}^w(k) - T_{\text{ch}}^c(k)}, \qquad (1)$$

where the subscript "ch" represents the channel number, $G_{\text{ch}}(k)$ is the gain function, $C_{\text{ch}}^s(k,i)$ stands for the scene count at the ith FOV of the kth scanline, $C_{\text{ch}}^c(k)$ and $C_{\text{ch}}^w(k)$ are the cold count and the warm count at the kth scanline, respectively, $T_{\text{ch}}^w(k)$ is the warm load temperature at the kth scanline, and $T_{\text{ch}}^c(k)$ is the cold space temperature that

is fixed at each channel. The overbar on $\overline{T}_{\text{ch}}^w$, $\overline{C}_{\text{ch}}^w$, and $\overline{C}_{\text{ch}}^c$ indicates a boxcar-smoothed warm load temperature, warm count, and cold count, respectively. The term $Q_{\text{ch}}(k,i)$ is a quadratic correction term, written as

$$Q_{\text{ch}}(k,i) = b_{0,\text{ch}}$$

$$\times \left\{ 1 - 4 \times \left[\frac{T_{b,\text{ch}}(k,i) - T_{\text{ch}}^c(k)}{T_{\text{ch}}^w(k) - T_{\text{ch}}^c(k)} - 0.5 \right]^2 \right\},$$

$$(2)$$

where $b_{0,\text{ch}}$ is a quadratic coefficient. Both the warm load temperature $T_{\text{ch}}^w(k)$ and the cold space temperature
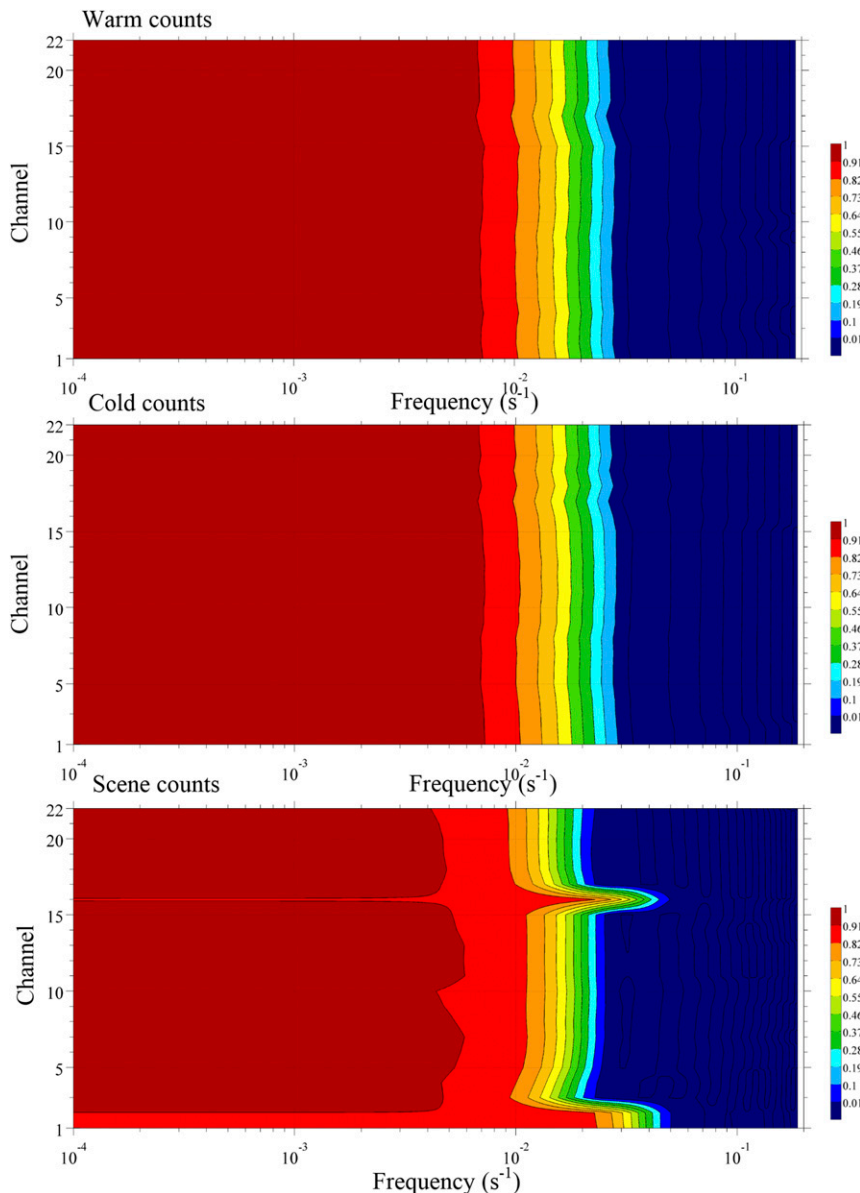
FIG. 7. Response functions for (top) warm counts, (middle) cold counts, and (bottom) scene counts calculated with the weighting coefficients in Fig. 5. Contours over dark blue shaded areas all have the value of 0.01 because of oscillations of the response functions.

$T_{ch}^{c}(k)$ have been corrected by ΔT_{ch}^{w} and ΔT_{ch}^{c}, respectively, to account for channel biases. Weng et al. (2013b) gave more details about the ATMS calibration process from raw data counts to antenna temperatures.

3. Methodology

a. The EEMD method

The method employed to extract the noise in the data series $\{C_{ch}^{w}(k)\}$, $\{C_{ch}^{c}(k)\}$, and $\{T_{ch}^{w}(k)\}$ $(k = 1, 2, \ldots, K)$ is the EEMD proposed by Wu and Huang (2009) where $C_{ch}^{w}(k)$, $C_{ch}^{c}(k)$, and $T_{ch}^{w}(k)$ stand for warm counts, cold

counts, and warm load temperatures in the kth scanline of channel as indicated by the subscript ch. The time series of these data are then decomposed into a set of IMFs:

$$C(k) = \sum_{m=l}^{L} \text{IMF}_m(k) + R_L(k), \qquad (3)$$

where R_L is the residual of the data $C(k)$ after the first L number of IMFs have been subtracted. In other words, the signals in the data series are decomposed successively from high frequencies to low frequencies. The first few IMFs describe the high-frequency noise. Therefore, the

warm count, cold count, and warm load temperature data series $\{C_{ch}^w(k)\}$, $\{C_{ch}^c(k)\}$, and $\{T_{ch}^w(k)\}$ ($k = 1, 2, \ldots, K$) can be smoothed by removing the first few high-frequency IMFs to obtain the EEMD-smoothed data series $\overline{C}_{ch}^{w,eemd}(k)$, $\overline{C}_{ch}^{c,eemd}(k)$, and $\overline{T}_{ch}^{w,eemd}(k)$ as follows:

$$\overline{C}_{ch}^{w,eemd}(k) = C_{ch}^w(k) - \sum_{m=l}^{L_w} \text{IMF}_m(k),$$

$$\overline{C}_{ch}^{c,eemd}(k) = C_{ch}^c(k) - \sum_{m=l}^{L_c} \text{IMF}_m(k),$$

$$\overline{T}_{ch}^{w,eemd}(k) = T_{ch}^w(k) - \sum_{m=l}^{L_T} \text{IMF}_m(k). \qquad (4)$$

The optimal filters for ATMS striping mitigation will be developed using these EEMD-smoothed warm count, cold count, and warm load temperatures $\overline{C}_{ch}^{w,eemd}(k)$, $\overline{C}_{ch}^{c,eemd}(k)$, and $\overline{T}_{ch}^{w,eemd}(k)$ as training samples.

b. Optimal symmetrical filters on warm counts and cold counts

Instead of using the EEMD-based method, we apply an optimal $(2N + 1)$ point filter to each of the data series $\{C_{ch}^w(k)\}$, $\{C_{ch}^c(k)\}$, and $\{T_{ch}^w(k)\}$ ($k = 1, 2, 3, \ldots, K$) to obtain three smoothed datasets $\{\overline{C}_{ch}^{w,opt}(k)\}$, $\{\overline{C}_{ch}^{c,opt}(k)\}$, and $\{\overline{T}_{ch}^{w,opt}(k)\}$:

$$\overline{C}_{ch}^{w,opt} = \sum_{n=-N}^{N} \alpha_n^w C_{ch}^w(k+n), \qquad (5a)$$

$$\overline{C}_{ch}^{c,opt} = \sum_{n=-N}^{N} \alpha_n^c C_{ch}^c(k+n), \qquad (5b)$$

$$\overline{T}_{ch}^{w,opt} = \sum_{n=-N}^{N} \alpha_n^T T_{ch}^w(k+n), \quad \text{and} \qquad (5c)$$

where α_n^w, α_n^c, and α_n^T ($n = 0, \pm 1, \ldots, \pm N$) are the optimal weighting coefficients for the optimal symmetrical filters on warm counts, cold counts, and warm load temperatures, and N is the total number of scanlines included in the filter. The effect of the filter defined in (5) on the data can be examined by comparing the power spectrum densities of the original data series with those of the smoothed series. Taking warm counts as an example, a Fourier transform is applied to both the original data sequence $\{C_{ch}^w(k)\}$ and the smoothed data sequence $\{C_{ch}^{w,opt}(k)\}$:

$$C_{ch}^w(k) = \sum_{m=0}^{K-1} f_m e^{-imk\beta}, \quad \text{and} \qquad (6a)$$

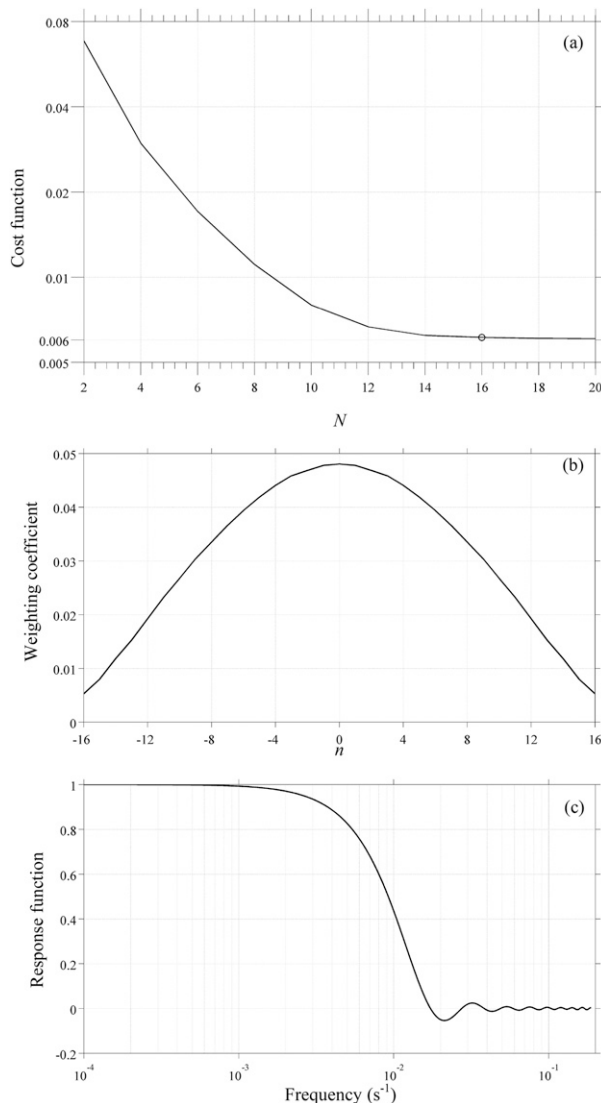$$C_{ch}^{w,opt}(k) = \sum_{m=0}^{K-1} \overline{f}_m e^{-imk\beta}, \qquad (6b)$$

FIG. 8. (a) Normalized cost function as a function of filter span N for the warm load temperature. The number of scanlines involved in the optimal filter is shown by the circle. (b) Weighting coefficients and (c) response function for warm load temperatures.

where $\beta = 2\pi/K$, m is the wavenumber ($m = 0, 1, \ldots, K - 1$), and f_m and $\overline{f}_m$ are Fourier coefficients that can be written as

$$f_m = \frac{1}{K} \sum_{k=0}^{K-1} C_{ch}^w(k) e^{-imk\beta}, \quad \text{and} \qquad (7a)$$

$$\overline{f}_m = \frac{1}{K} \sum_{k=0}^{K-1} \overline{C}_{ch}^{w,opt}(k) e^{-imk\beta}. \qquad (7b)$$

The ratio r_m of the Fourier coefficient of the filtered data series $\overline{f}_m$ to the Fourier coefficient of the filtered data series f_m can then be written as
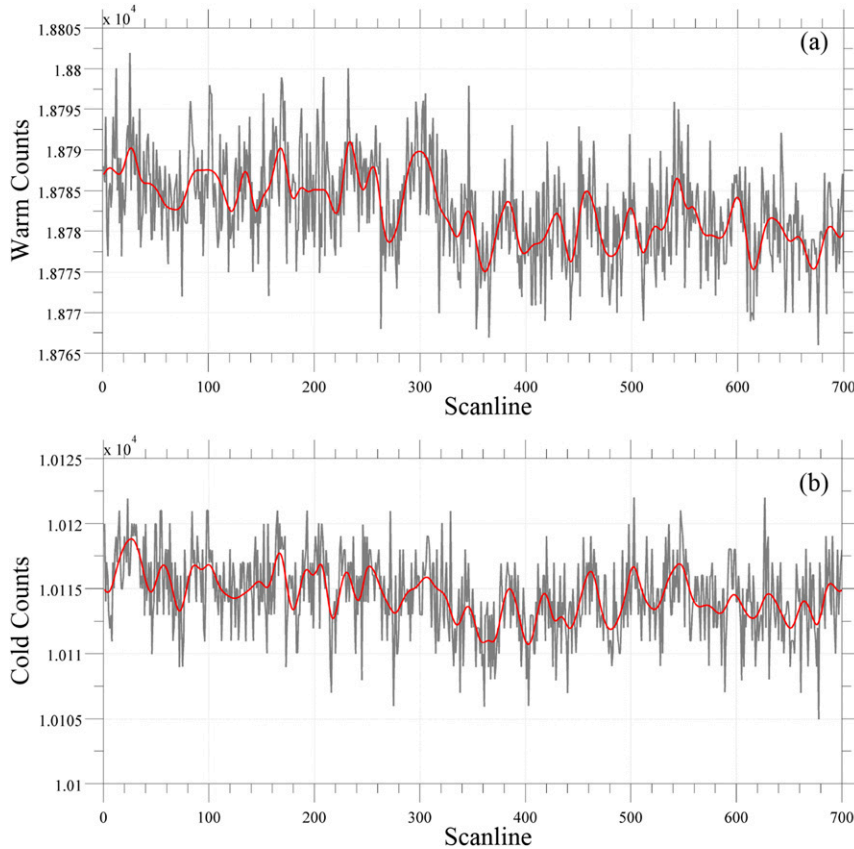
FIG. 9. Variations in (a) warm counts and (b) cold counts along 700 scanlines (i.e., a swath between $\pm 55°$N) before (gray lines) and after (red lines) removing three IMFs at channel 8.

$$r_m = \frac{\overline{f}_m}{f_m}. \tag{8}$$

The ratio r_m is called the spectral response function of the filter defined in (5). In the case of a symmetrical filter where $\alpha_n = \alpha_{-n}$, (5a) can be written as

$$\overline{C}_{\text{ch}}^{w,\text{opt}}(k) = \frac{1}{2} \sum_{n=0}^{N} \alpha_n [C_{\text{ch}}^w(k-n) + C_{\text{ch}}^w(k+n)]. \tag{9}$$

Substituting (6a) and (7a) into (9), we obtain

$$\overline{C}_{\text{ch}}^{w,\text{opt}} = \frac{1}{K} \sum_{k=0}^{K-1} \frac{1}{2} \sum_{n=0}^{N} \alpha_n [C_{\text{ch}}^w(k-n) + C_{\text{ch}}^w(k+n)] e^{-imk\beta}$$

$$= \sum_{n=0}^{N} \alpha_n \cos(mn\beta) f_m. \tag{10}$$

Substituting (10) into (8), we then obtain an analytic expression for the spectral response function r_m:

$$r_m = \sum_{n=0}^{N} \alpha_n^w \cos(mn\beta). \tag{11}$$

The weighting coefficients for the symmetric filter for warm counts are obtained by requiring that the filter-smoothed warm counts approximately equal the EEMD-smoothed ones; that is,

$$\begin{cases} \min J = \min \sum_{k=1}^{K} \left[\sum_{n=-N}^{N} \alpha_n^w C_{\text{ch}}^w(k+n) - \overline{C}_{\text{ch}}^{w,\text{eemd}}(k) \right]^2, \\ \sum_{n=-N}^{N} \alpha_{\text{ch}}^w = 1. \end{cases} \tag{12}$$

The constraint minimization problem in (12) is solved using the Lagrange method:

$$\begin{cases} L(\alpha_n^w, \lambda) = J + \lambda \left(1 - \sum_{n=-N}^{N} \alpha_n^w \right), \\ \dfrac{\partial L}{\partial \alpha_{\text{ch}}^w} = 0, \dfrac{\partial L}{\partial \lambda} = 0. \end{cases} \tag{13}$$

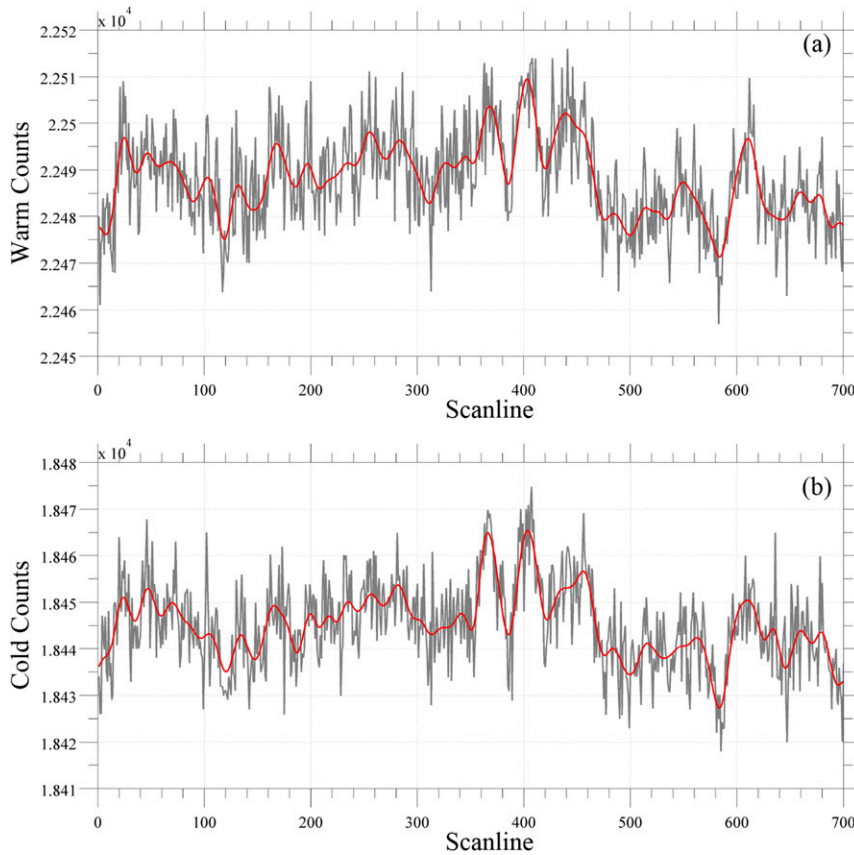Similar procedures are also applied to cold counts and warm load temperatures.

FIG. 10. As in Fig. 9, but for channel 22.

c. Optimal symmetrical filters for scene counts

Different from warm counts, cold counts, and warm load temperatures, scene counts vary not only in the along-track direction but also in the cross-track direction. The striping noise remains nearly constant in the along-track direction. A PCA is first done to extract the first PCA component so that the primary scan-dependent features in the scene counts can be captured. The EEMD- and optimal-filtering approaches are applied to the first PCA component. The data matrix for the PCA analysis of scene counts can be expressed as

$$C_{M \times N}^{s} = \begin{pmatrix} C_{1,1}^{s} & C_{1,2}^{s} & \cdots & C_{1,N}^{s} \\ C_{2,1}^{s} & C_{2,2}^{s} & \cdots & C_{2,N}^{s} \\ \vdots & \vdots & \ddots & \vdots \\ C_{M,1}^{s} & C_{M,2}^{s} & \cdots & C_{M,N}^{s} \end{pmatrix}, \qquad (14)$$

where M is the total number of scanlines, and N is the total number of FOVs. The scene counts at the ith FOV of the kth scanline $C_{k,i}^{s}$ can then be expressed as (Qin et al. 2013)

$$C_{k,i}^{s} = \sum_{j=1}^{96} e_{j,i} u_{k,j}, \qquad (15)$$

where $e_{j,i}$ is the ith (scan position) element of the jth PC mode $\mathbf{e}_j$, and $u_{k,j}$ is the kth (scanline) element of the jth PC coefficient $\mathbf{u}_j^{\mathrm{T}}$. The first L IMFs of the first PC coefficient, describing the high-frequency striping noise, are removed, and the remaining PCA components are kept the same to obtain the EEMD-smoothed scene counts:

$$\overline{C}_{i,k}^{s,\mathrm{eemd}} = e_{i,1} \left[u_{1,k} - \sum_{m=1}^{L} I\mathrm{MF}_m(k) \right] + \sum_{j=2}^{96} e_{i,j} u_{j,k}. \qquad (16)$$

A $(2N + 1)$-point filter can be applied to obtain a filter-smoothed scene count data series $\{\overline{C}_{i,k}^{s,\mathrm{opt}}\}$ as follows:

$$\overline{C}_{k,i}^{s,\mathrm{opt}} = \sum_{n=-N}^{N} \alpha_n^s e_{i,1} u_{1,k+n} + \sum_{j=2}^{96} e_{i,j} u_{j,k}, \qquad (17)$$

where α_n^s $(n = 0, \pm 1, \ldots, \pm N)$ are the optimal weighting coefficients for the scene counts using a procedure similar to that described in section 3b.
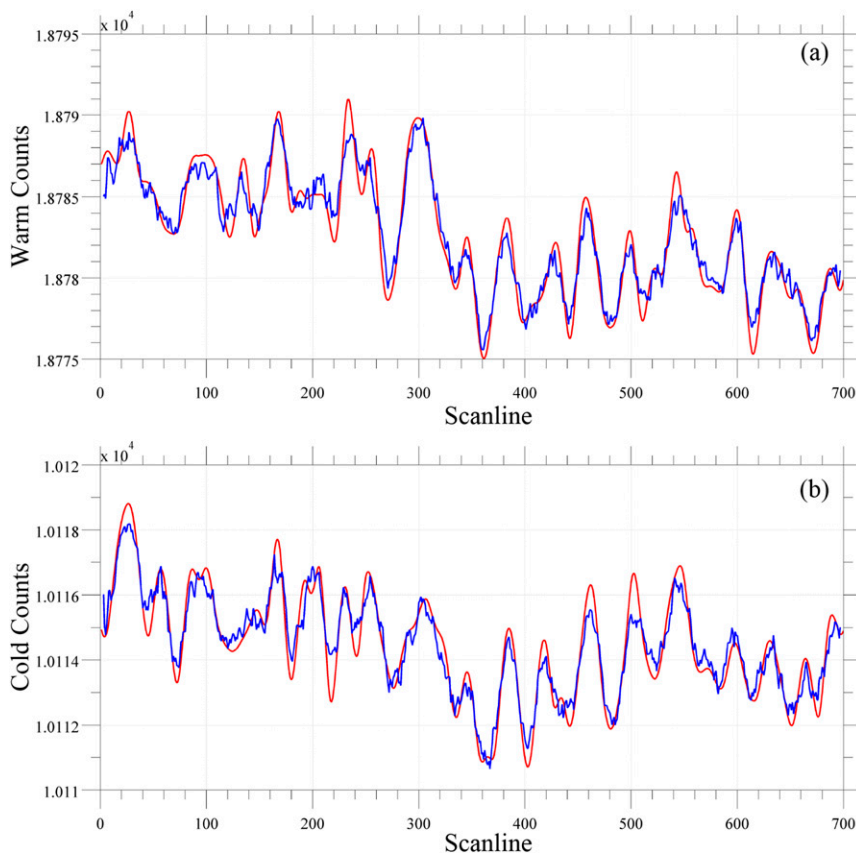
FIG. 11. Variations in (a) warm counts and (b) cold counts with the optimal filter (red lines) and 17-point smoothing (blue lines) for channel 8.

4. Numerical results

a. Spectrum analyses of IMFs of calibration counts

Data series of warm counts, cold counts, warm load temperatures, and the first PC coefficient of scene counts for all ATMS channels within 55°S–55°N on 24 February 2012 were decomposed into a series of IMFs. Figure 2 shows the Fourier spectra of the first six IMFs as a function of frequency for warm counts and cold counts at channel 8. As the IMF number increases, its peak amplitude is located at increasingly lower frequencies. Noise at high frequencies is captured in the first few IMFs, and large-scale variations are captured in the remaining IMFs. The main criterion to decide which IMFs are noise, or how many IMFs to remove, is whether the peak amplitude of a certain IMF continues to decline. At the beginning of the fourth IMF for both warm counts and cold counts, the peak amplitude is no longer smaller than that of the previous IMFs. So the first three IMFs are primarily noise signals. The magnitudes of the first three IMFs at low frequencies are small, suggesting that removing the first three IMFs will not change the warm count or cold count features at low

frequencies. Results obtained for the other 21 ATMS channels are similar (not shown). Therefore in this study, the first three IMFs are removed for both warm counts and cold counts at all ATMS channels.
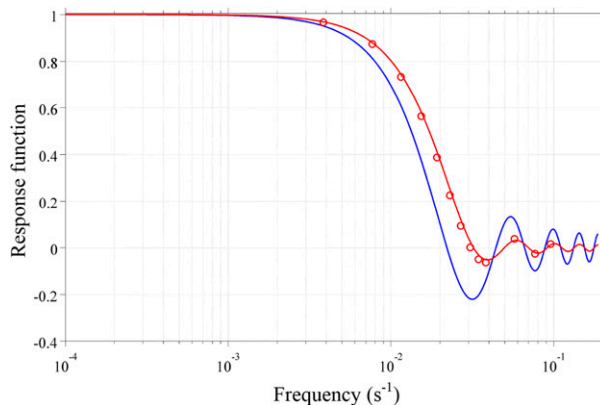

FIG. 12. Variations in the response function as a function of frequency for the 17-point filter (blue line) and the optimal filter (red line) applied to warm counts of channel 8. The red circles show the response function for channel 12 after application of the optimal filter. The response functions for the cold counts are the same as those shown here (figure omitted).
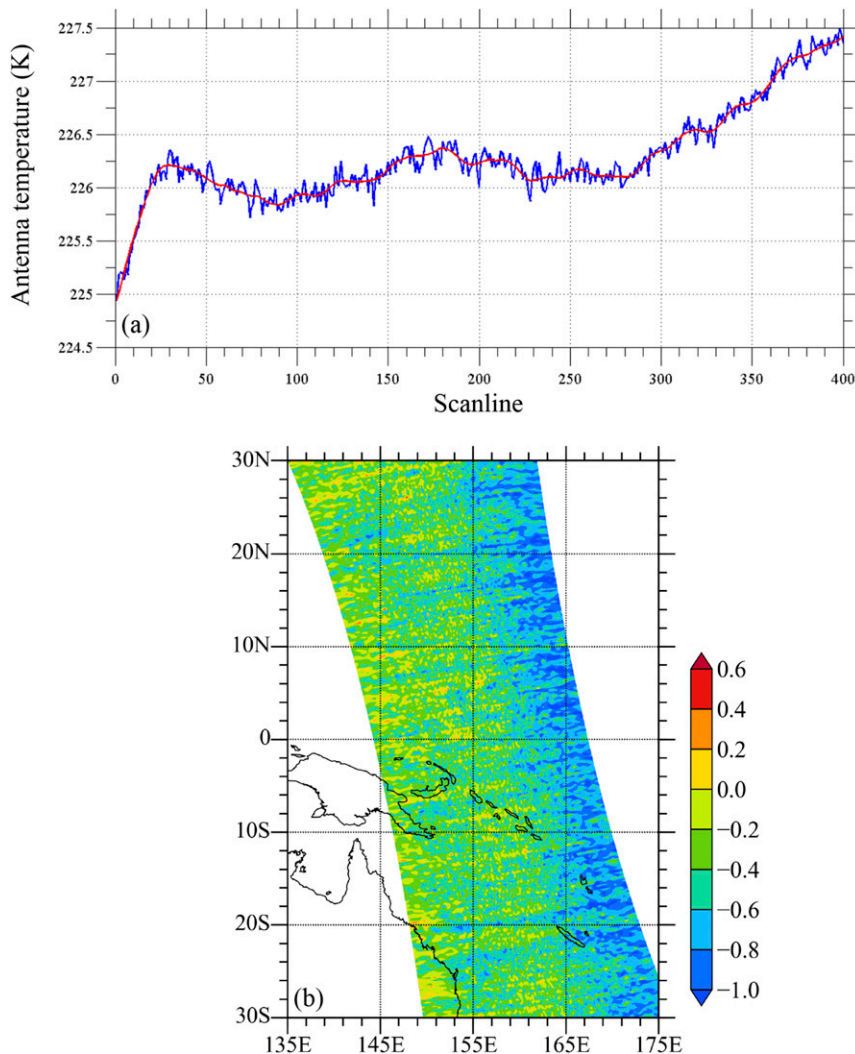
FIG. 13. (a) Variations in antenna temperature for channel 8 at nadir with (red) and without (blue) applying the optimal filter on the scene counts. Warm counts, cold counts, and warm load temperatures are all smoothed. (b) Antenna temperatures at channel 8 without smoothing scene counts.

Figure 3 shows the Fourier spectra of the first six IMFs for warm load temperatures. Note that the fifth and sixth IMFs peak at the same frequency but that the amplitude of the sixth IMF is smaller than that of the fifth IMF. This suggests that no significant signal can be found at lower frequencies starting from the sixth IMF. Unlike warm counts or cold counts that change only in the along-track direction, ideal warm load temperatures should have constant values, implying zero Fourier spectra for the true signal. Thus, a total of five IMFs are removed from warm load temperatures. Figure 4 shows the Fourier spectra of the first six IMFs of the first PC coefficient for scene counts at channel 8. The fourth IMF has much larger magnitudes than the third IMF at both the peak and low frequencies. Therefore, removing the first three IMFs is enough to eliminate the noise while keeping the large-scale information. A similar analysis was carried out for all 22 channels. Table 1 lists the total number of IMFs removed from scene counts for each ATMS channel. For ATMS window channels 1–2 and 16, only two IMFs need to be removed because two IMFs are sufficient to capture the data noise. For the remaining channels, three IMFs are removed.

b. Properties of the optimal symmetrical filters

As described in sections 3 and 4, the EEMD-smoothed warm counts, cold counts, warm load temperatures, and scene counts are then taken as training samples to establish the optimal filters expressed in (5) and (17).

To decide on the filter span N, weighting coefficients and cost functions of $(2N + 1)$ point symmetrical optimal filters with different spans ranging from 2 to 30 were calculated. Cost functions describe how close the counts smoothed by EEMD are to those by the optimal filter and have different magnitudes at different channels. Figure 5 shows variations in the normalized cost functions of the optimal filters as a function of filter span for warm counts, cold counts, and scene counts at all ATMS channels. The cost functions drop rapidly as the filter span N increases, suggesting that the optimal filters tend to capture the EEMD features more closely if more scanlines are involved. The goal is to remove striping noise with the least number of scanlines in the optimal filter. The black circles in Fig. 5 indicate the selected filter spans of the optimal filters (see also Table 1). Surface channels have narrower filters mainly because there are only two IMFs removed, making changes to the counts data smaller. Temperature-sounding channels have wider filters than humidity-sounding channels for warm counts and cold counts, but narrower filters for scene counts.

Figure 6 shows weighting coefficients of the optimal filters for warm counts, cold counts, and scene counts at all channels. All weighting coefficients have symmetrical parabolic shapes. This suggests that data points with identical distances to the filtering point weigh exactly the same within any filter. Also, those closer to the filtering point ($n = 0$) are weighted more than data points farther away. The filtering points themselves appear to have the greatest importance, while data points farther away have less impact on the smoothed counts, which is reasonable. Weighting coefficients with the same distance to the filtered points have similar magnitudes for warm counts and cold counts at different channels. Scene counts at channels 1–2 and 16 have larger weighting coefficients than those for the other channels because the sum of the weighting coefficients of any filter is unity, and fewer scanlines are involved in these three window channels.

Figure 7 shows the spectral response functions calculated with the optimal weighting coefficients shown in Fig. 6 according to (11). For warm counts, cold counts, and scene counts at all channels, the response functions are ~1 until they drop sharply to around zero at ~10^{-2} s^{-1}. The magnitudes of low-frequency signals are thus not altered, and the high-frequency noise is significantly reduced. The counts data at low frequencies are not changed much by the optimal filters. Also, the majority of noise removed centered around 10^{-2} s^{-1}. This implies that the optimal filters remove striping information while retaining large-scale signals. The contours over the dark
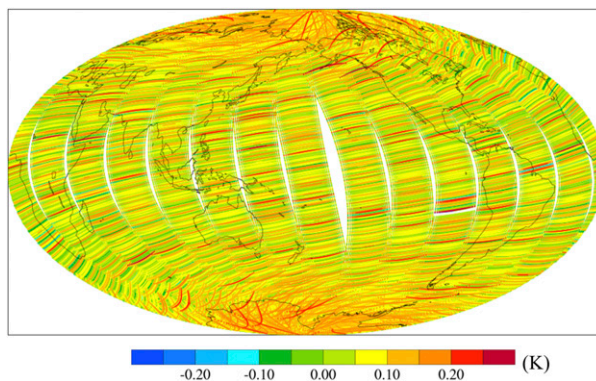

FIG. 14. Striping noise (K) removed by the optimal symmetric filter for ATMS channel 8 at the ascending node on 24 Feb 2012.

blue shaded areas all have the value of 0.01 because of the oscillations in response function values. For scene counts, the response functions at window channels 1–2 and 16 decrease from 1 to 0 at higher frequencies, suggesting that more signals are retained. It agrees with the fact that only two IMFs are removed, compared to three IMFs at other channels. Although corrections might be different among ATMS channels, warm load temperatures do not change as the channel number changes. Figure 8 shows the cost functions, weighting coefficients, and response functions for warm load temperatures.

c. Comparison between the optimal filters and the boxcar filters

Figures 9 and 10 show the warm counts and cold counts before and after application of optimal filters at channels 8 and 22, respectively. After the optimal filters are applied, warm counts and cold counts become much smoother without any visible noise at both channels while the larger-scale variations are kept, proving the effectiveness of the optimal filters. Conventionally, 17-point boxcar filters are used to smooth warm counts and cold counts. Figure 11 shows the variations in warm counts and cold counts after applying both the optimal filter and the boxcar filter. Compared with the optimal filter, the boxcar filter fails to smooth out all visible noise and significantly reduces the magnitudes of the minimum and maximum values.

Response functions for channel 8 after application of the boxcar filter and the optimal filter, both with the same filter widths of 8, were also calculated. Figure 12 shows that the response function for the optimal filter falls from 1 to around 0 when the frequency increases. The magnitudes of low-frequency signals remain constant while those of high frequencies are
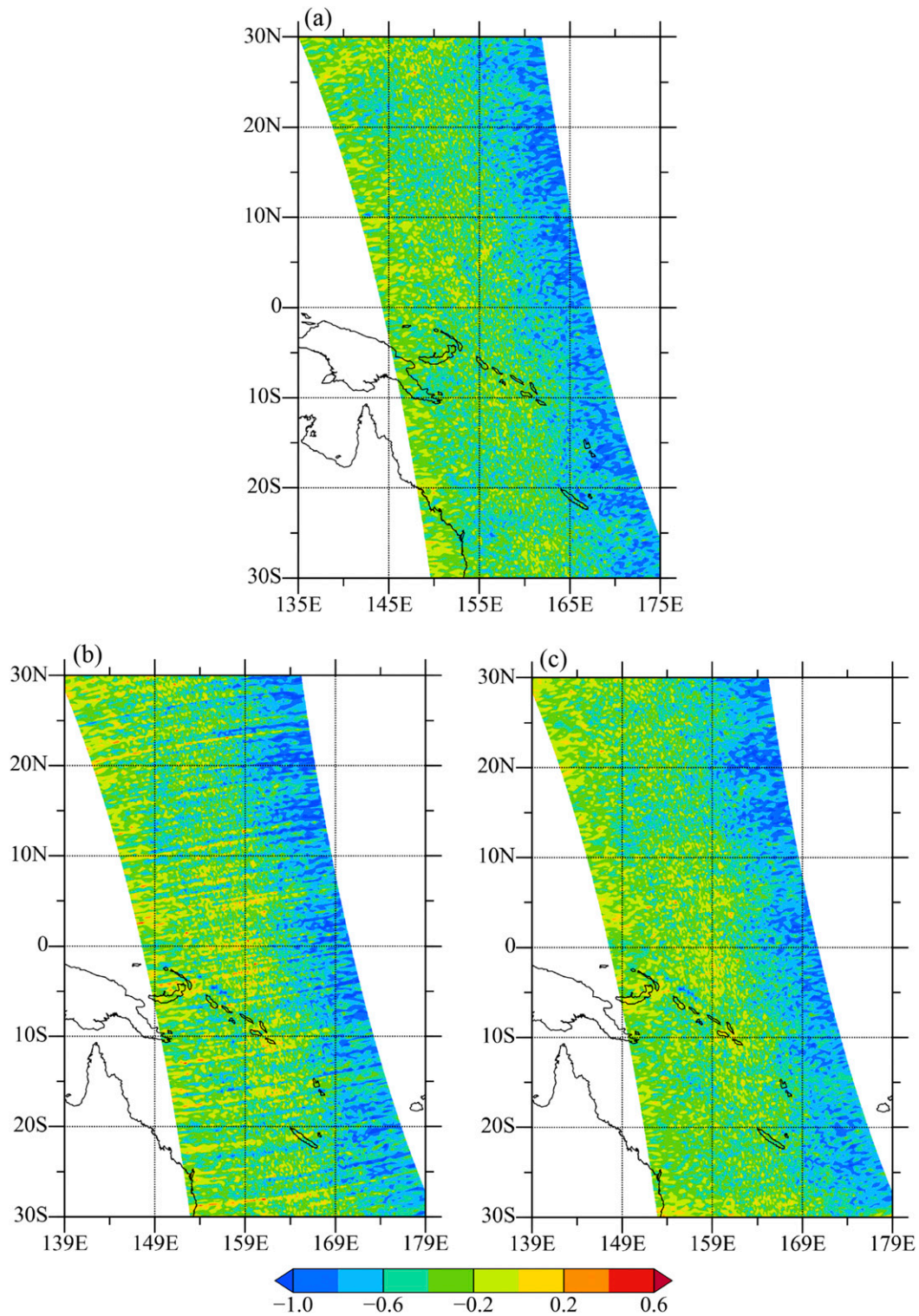
FIG. 15. (a) ATMS channel-8 antenna temperature differences between observations and model simulations (i.e., $O - B$) on 24 Feb 2012 after the destriping using the optimal symmetric filter. ATMS channel-8 antenna temperatures between observations and model simulations (i.e., $O - B$) on 1 Mar 2012 (b) before and (c) after the destriping using the optimal symmetric filter.

significantly reduced. The response function for the boxcar filter starts to decrease sharply at frequencies lower than $10^{-2}\,s^{-1}$, implying that the boxcar filter suppresses low-frequency signals that should be retained. Another problem is that in the high-frequency range, where the major part of the noise still exists, the oscillatory behavior of the response function of the boxcar filter hinders this filter from completely removing the actual data noise.

d. The effects of optimal filters on antenna temperatures

Smoothed warm counts, cold counts, and warm load temperatures are commonly used to calculate antenna temperatures. Scene counts are not smoothed. Figure 13 shows antenna temperatures for ATMS channel 8 at nadir calculated with and without applying the optimal filter to scene counts. Warm counts, cold counts, and warm load temperatures are all smoothed here using the optimal filter. Even if noise in the warm counts, cold counts, and warm load temperatures are effectively smoothed out, antenna temperatures are still contaminated with striping noise if the scene counts are not smoothed (Fig. 13b). This confirms the necessity of smoothing the scene counts.

Figure 14 shows the global distributions of the striping noise extracted from antenna temperatures for ATMS channel 8. The destriping algorithm is also applicable to observations on other times. Figure 15 gives the regional distributions of the $O - B$ differences in ATMS channel-8 antenna temperatures before (Fig. 1b) and after destriping on 24 February 2012 (Fig. 15a) and 1 March 1 2012 (Figs. 15c,d). The striping noise is ~0.3 K for channel 8, which agrees well with the results described by Qin et al. (2013). Striping patterns are faintly visible in the $O - B$ field before destriping (Fig. 15b). These striping patterns are much less visible after destriping (Fig. 15c).

5. Summary and conclusions

An along-track striping phenomenon has been detected in global $O - B$ distributions of ATMS temperature-sounding channels. The EEMD method is typically employed to characterize the noise in warm counts, cold counts, warm load temperatures, and scene counts. However, this method is not convenient for operational applications. The development of a set of optimal filters that can reduce noise in calibration counts as efficiently as the EEMD does is thus desirable. The conventionally used boxcar filters in satellite calibration tend to alter low-frequency weather signals when suppressing high-frequency noise. In this study, four sets of optimal symmetrical filters were designed and developed for the calibration counts of all 22 ATMS channels. The optimal filters efficiently removed striping noise within antenna temperatures while keeping the large-scale features intact. The necessity of smoothing the scene counts is further confirmed. If calibration counts are smoothed but scene counts are not, the striping noise will still exist and remain visible in global $O - B$ distributions. Further investigation into the root cause of the striping noise is needed and impacts of striping noise on ATMS data applications in NWP and climate studies will be reported on in follow-on papers.

REFERENCES

Bormann, N., A. Fouilloux, and W. Bell, 2013: Evaluation and assimilation of ATMS data in the ECMWF system. *J. Geophys. Res. Atmos.*, **118**, 12 970–12 980, https://doi.org/10.1002/2013JD020325.

GSFC, 2011: Joint Polar Satellite System (JPSS) Advanced Technology Microwave Sounder (ATMS) SDR radiometric calibration. Joint Polar Satellite System Algorithm Theoretical Basis Doc., 41 pp., https://jointmission.gsfc.nasa.gov/sciencedocs/2015-06/474-00043_Rev-Baseline.pdf.

Kim, E., C.-H. J. Lyu, K. Anderson, R. V. Leslie, and W. J. Blackwell, 2014: S-NPP ATMS instrument prelaunch and on-orbit performance evaluation. *J. Geophys. Res. Atmos.*, **119**, 5653–5670, https://doi.org/10.1002/2013JD020483.

Qin, Z., X. Zou, and F. Weng, 2013: Analysis of ATMS striping noise from its Earth scene observations. *J. Geophys. Res. Atmos.*, **118**, 13 214–13 229, https://doi.org/10.1002/2013JD020399.

Tian, X., and X. Zou, 2016: ATMS- and AMSU-A-derived hurricane warm core structures using a modified retrieval algorithm. *J. Geophys. Res. Atmos.*, **121**, 12 630–12 646, https://doi.org/10.1002/2016JD025042.

——, and ——, 2018: Capturing size and intensity changes of Hurricanes Irma and Maria (2017) from polar-orbiting satellite microwave radiometers. *J. Atmos. Sci.*, **75**, 2509–2522, https://doi.org/10.1175/JAS-D-17-0315.1.

——, ——, and N. Sun, 2018: Comparison of RO-estimated ATMS biases between NOAA-20 and S-NPP. *Int. Geoscience and Remote Sensing Symp.*, Valencia, Spain, IEEE, 3093–3096, https://doi.org/10.1109/IGARSS.2018.8519416.

Weng, F., X. Zou, X. Wang, S. Yang, and M. Goldberg, 2012: Introduction to Suomi National Polar-Orbiting Partnership Advanced Technology Microwave Sounder for numerical weather prediction and tropical cyclone applications. *J. Geophys. Res.*, **117**, D19112, https://doi.org/10.1029/2012JD018144.

——, H. Yang, and X. Zou, 2013a: On convertibility from antenna to sensor brightness temperature for ATMS. *IEEE Geosci.*

Remote Sens. Lett., **10**, 771–775, https://doi.org/10.1109/LGRS.2012.2223193.

——, and Coauthors, 2013b: Calibration of Suomi National Polar-Orbiting Partnership Advanced Technology Microwave Sounder. *J. Geophys. Res. Atmos.*, **118**, 11 187–11 200, https://doi.org/10.1002/jgrd.50840.

Wu, Z., and N. E. Huang, 2009: Ensemble empirical mode decomposition: A noise-assisted data analysis method. *Adv. Adapt. Data Anal.*, **1**, 1–41, https://doi.org/10.1142/S1793536909000047.

——, ——, and X. Chen, 2009: The multi-dimensional ensemble empirical mode decomposition method. *Adv. Adapt. Data Anal.*, **1**, 339–372, https://doi.org/10.1142/S1793536909000187.

Zou, X., and X. Tian, 2018: Hurricane warm-core retrievals from AMSU-A and remapped ATMS measurements with rain contamination eliminated. *J. Geophys. Res. Atmos.*, **123**, 10 815–10 829, https://doi.org/10.1029/2018JD028934.

——, and ——, 2019: Comparison of ATMS striping noise between NOAA-20 and S-NPP and noise impact on warm core retrieval of Typhoon Jelawat (2018). *IEEE J. Sel. Top. Appl. Earth Obs. Remote Sens.*, https://doi.org/10.1109/JSTARS.2019.2891683, in press.

——, F. Weng, B. Zhang, L. Lin, Z. Qin, and V. Tallapragada, 2013: Impacts of assimilation of ATMS data in HWRF on track and intensity forecasts of 2012 four landfall hurricanes. *J. Geophys. Res. Atmos.*, **118**, 11 558–11 576, https://doi.org/10.1002/2013JD020405.

——, L. Lin, and F. Weng, 2014: Absolute calibration of ATMS upper level temperature sounding channels using GPS RO observations. *IEEE Trans. Geosci. Remote Sens.*, **52**, 1397–1406, https://doi.org/10.1109/TGRS.2013.2250981.

——, H. Dong, and Z. Qin, 2017: Striping noise reduction for ATMS window channels using a modified destriping algorithm. *Quart. J. Roy. Meteor. Soc.*, **143**, 2567–2577, https://doi.org/10.1002/qj.3107.